In-situ cation-exchange strategy for engineering single-atomic Co on TiO$_2$ photoanode toward efficient and durable solar water splitting

Kai Song [a,b,c,d], Huilin Hou [a,*], Dongdong Zhang [a], Fang He [b,c,**], Weiyou Yang [a,*]

[a] Institute of Micro/Nano Materials and Devices, Ningbo University of Technology, Ningbo 315211, PR China
[b] School of Materials Science and Engineering, Tianjin University, Tianjin 300350, PR China
[c] Tianjin Key Laboratory of Composite and Functional Materials, Tianjin University, Tianjin 300350, PR China
[d] Department of Physics, Taiyuan University of Science and Technology, Taiyuan 030024, PR China

ARTICLE INFO

ABSTRACT

Single-atomic catalysts (SACs) have been emerging as one of potential candidates in catalysts, owing to their unique merits with extremely high specific surface area as well as remarkably exposed active sites. Herein, we develop an *in-situ* gas-phase cation exchange strategy for engineering single-atomic Co on the surface of TiO$_2$ photoanode toward solar water splitting. It is verified that the atomically-dispersed Co with Co-O coordination could optimize the surface electronic structures, enhance the light absorption, promote the photoinduced charge transfer, lower the reaction barrier and accelerate the reaction kinetics, which consequently enable the overall improved photoelectrochemical (PEC) behaviors for photoanodes. As a proof of concept, the as-constructed TiO$_2$-based photoanodes deliver robust stability up to 100 h and a photocurrent density up to 1.47 mA cm^{-2} at 1.23 V *vs.* RHE, which are superior to those of pristine TiO$_2$, representing their significance for potential applications.

1. Introduction

Recently, the green hydrogen energy has been deemed as one of the best choices to alternative fossil fuels, due to its pro-environment, light-weight and well-stocked specialty [1,2]. It is well-known that one of the exciting ways to extract hydrogen is splitting water into oxygen and hydrogen [3–5]. To date, various water splitting techniques have been developed to produce hydrogen, such as electrocatalysis [6], photo-catalysis [7,8], photoelectrochemical (PEC) [9] and photochemical [10] methods. Particularly, PEC water splitting is recognized as one of the most promising ways to generate hydrogen in a clean and sustainable manner driven by solar energy [11–14].

In general, PEC water splitting technique often requires photoactive electrodes (either photoanode or photocathode) in an electrochemical cell to generate H$_2$ and O$_2$ under light irradiation [15,16]. Typically, the four-electron oxygen evolution reaction (OER) that occurs on the surface of photoanode is often the bottleneck due to its high reaction barrier [2,17]. Accordingly, it is highly desired to develop an efficient photoanode with reduced reaction barrier for high PEC performance. Since the discovery of PEC water splitting in 1972 [18], various favorable photo-anodes have been explored for PEC water splitting, such as TiO$_2$

[19–22], BiVO$_4$ [1,23–28], WO$_3$ [29], Fe$_2$O$_3$ [30], Ta$_3$N$_5$ [31]. Amongst, TiO$_2$ is considered as one of the most promising candidates, attributed to its suitable valence-band position, nontoxicity, superior photochemical stability and low cost [32,33]. However, the PEC performance of TiO$_2$-based photoanodes is often unsatisfied, which could be mainly ascribed to their intrinsic poor charge transport, sluggish OER kinetics, as well as the limited light absorption [34].

Over the past decades, extensive efforts have been devoted to over-coming those problems as mentioned above, mainly including morphology and defect engineering [11,35], doping [36], hetero-junction construction [37] and cocatalysts assistance [38]. Most recently, the strategy based on single-atom catalysts (SACs, namely, isolated metal atoms anchored on the supports), are emerging as one of idea candidates in catalysts. In comparison to the conventional coun-terparts, SACs often possess the unique merits of much higher specific surface area and remarkably exposed active sites [39–42]. For instance, Zhang et al. developed a versatile strategy to engineer atomically-dispersed Ni-N$_4$-O sites on BiVO$_4$/OEC-based photoanode for enhanced PEC performance [28]. Nevertheless, there were scarce work shed light on the application of SACs in PEC water splitting, which might be mainly attributed to the fact that directly building SACs on/in the

---

photoanodes is not an easy case [43].

In current work, we develop a facile strategy based on *in-situ* gas-phase cation exchange for engineering single-atomic Co on the surface of TiO$_2$ photoanode toward efficient and durable solar water splitting. It is verified that the incorporated single-atom Co could prominently alter the electronic structures of TiO$_2$ photoanode for promoting visible-light absorption and facilitating the holes transfer. Furthermore, the Co atom on the surface of TiO$_2$ act as active sites for substantially reducing the OER energy barrier, as disclosed by the DFT analyses. As a result, the as-prepared Co/TiO$_2$ photoanodes achieve a high photocurrent density of 1.47 mA cm^{-2} at 1.23 V *vs.* RHE, which is 3.1 times to that of pristine TiO$_2$ and exceeds those of most TiO$_2$-based analogues ever reported. Moreover, they behave long-term stability up to 100 h, underscoring their significance for potential applications.

2. Experimental section

2.1. Reagents and materials

Fluorine-doped tin oxide (FTO, < 22 Ω/sq) coated glass as current collector and substrates were purchased from Yingkou Opivite New Energy Technology Co., Ltd. China. Titanium (IV) butoxide (C$_{16}$H$_{36}$O$_4$Ti , 98%), concentrated HCl (38 wt%) were bought from Aladdin Reagent Co., Ltd. (Shanghai, China). Cobalt chloride hexahydrate (CoCl$_2$·6 H$_2$O, 99%), sodium sulfate (Na$_2$SO$_4$), sulfuric acid (H$_2$SO$_4$), potassium hydroxide (KOH) and sodium sulfite (Na$_2$SO$_3$) were purchased from Sinopharm Chemical Reagent Company. All chemicals were used directly without any further purification. The used deionized water is self-made.

2.2. Preparation of the photoanodes

2.2.1. Pristine TiO$_2$ photoanodes

TiO$_2$ nanowire (NW) arrays on FTO glass were synthesized using a typical hydrothermal method [44,45]. Briefly, 0.35 mL of titanium (IV) butoxide was added into 30 mL of an aqueous HCl solution (15 mL deionized (DI) water mixed with 15 mL concentrated HCl (38 *wt.*%)) under magnetic stirring. The autoclave was sealed and heated to 150 °C for 8 h in an electric oven. The obtained TiO$_2$ sample was annealed in air at 450 °C for 2 h.

2.2.2. Co/TiO$_2$ photoanodes

The obtained TiO$_2$ photoanode was then placed in the center of a quartz tube (50 mm in diameter) while CoCl$_2$ powder was placed at ~4 cm upstream from the center of quartz tube. After the system is vacuumed, N$_2$ gas was introduced and kept flowing flowed in the system (50 sccm). The furnace was heated up to the desried temperatures of 360, 380, 400, and 420 °C with a heating rate of 20 °C min^{-1} and maintained for 2 min, respectively. The CoCl$_2$ and TiO$_2$ have different roles in our present experiment, in which CoCl$_2$ is the replacement source and TiO$_2$ is the replacement template. Under low vacuum environment, the occurrence of gas-phase cation reactions does not need to reach the thermodynamic melting point of the material. Although CoCl$_2$ is stable with a melting point of 737 °C and a boiling point of 1049 °C, CoCl$_2$ vapor could be generated at a relatively low temperature under vacuum environment, which can guarantee the smooth operation of cation exchange reaction. At this lower temperature, TiO$_2$ can keep the initial stable structure due to its high melting point of 1850 °C. In brief, the reaction process can be described by the followed equation:

TiO$_2$(solid) + CoCl$_2$(vapor) → TiCo$_x$O$_{2-x}$ (solid) + TiCl$_y$(vapor) + O$_2$(vapor)·
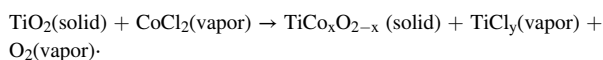
It is clear that the replaced Ti would form chlorides vapor (TiCl$_y$), which would be carried away from the furnace by continuously flowed N$_2$. Subsequently, the furnace cools naturally to room temperature. To remove the residual CoCl$_2$, all samples were cleaned many times after gas phase cation replacement reaction. Accordingly, the obtained products were referred to as Co/TiO$_2$-360, Co/TiO$_2$-380, Co/TiO$_2$-400, Co/TiO$_2$-420, respectively. For comparison, the TiO$_2$ photoanodes with oxygen vacancies (TiO$_2$-Ov) were also prepared by the same process of Co/TiO$_2$ samples without introduction of CoCl$_2$ in the furnace.

2.3. Characterization

Scanning electron microscopy (SEM) measurements were characterized by Hitachi S-4800. EDX is performed under a Bruker energy spectrometer equipped in SEM. Transmission electron microscopy (TEM) measurements were carried out by using JEM-2100 F microscope operated at 200 kV. The X-ray diffraction (XRD) patterns were recorded on Bruker X-ray diffractometer equipped with Cu-Kα radiation (40 thousand volts, 20 mA). The X-ray photoelectron spectroscopy (XPS) was carried out in the Thermal-fish photo-electron spectrometer. The UV–vis diffuse reflectance spectra were performed on a UV-3100 spectrometer by using BaSO$_4$ as reference.

2.4. PEC measurements

The photoelectrochemical (PEC) properties were measured by an electrochemical analyzer (CHI760D) in a standard three-electrode system. 1 M KOH aqueous solution (pH = 13.6) was used as an electrolyte for PEC measurements. The illumination sourc was simulated sunlight with a xenon lamp coupled with an AM 1.5 global filter (100 mW cm^{-2}). The current-potential (*J-V*) characteristics were recorded by scanning the potential a scan rate of 10 mV s^{-1}. The measured potentials *vs.* Ag/AgCl were converted to the reversible hydrogen electrode (RHE) scale using the relationship of $E_{RHE} = E_{Ag/AgCl} + 0.059 *pH + 0.197$ (at 20 °C). The incident photon-to-current conversion efficiency (IPCE) was measured at 1.23 V$_{RHE}$ in 1 M KOH solution by using the same three-electrode setup as described above, which can be set as:

IPCE= 1240 × I(mA/cm^2) / (Plight (mW/cm^2) × λ(nm))

where *I* is the measured photocurrent density at specific wavelength, *λ* is the wavelength of incident light, and *P$_{light}$* is the measured light power density, respectively. Giving 100% Faradaic efficiency, the applied bias photon-to-current efficiency (ABPE) can be calculated by:

ABPE = I(mA/cm^2) × (1·23 - V$_{bias}$) (V) / Plight (mW/cm^2)

in which *I* was the photocurrent density, *V$_{bias}$* is the applied potential, *P$_{light}$* is the incident illumination power density (100 mW cm^{-2}), respectively. The electrochemical impedance spectroscopy (EIS) Nyquist plots were obtained at 1.23 V (*vs.* RHE) with small AC amplitude of 10 mV in the frequency range from 10^{-2} to 10^5 Hz.

The charge injection efficiency (η$_{injection}$) can be calculated by:

η$_{injection}$ = J$_{water}$ / J$_{sulfite}$

The charge separation efficiency (η$_{separation}$) can be calculated by:

η$_{separation}$ = J$_{sulfite}$ / J$_{abs}$.

Photoelectrochemical H$_2$ and O$_2$ evolutions were studied in 1 M KOH after saturation with N$_2$ gas for 30 min. The evolved H$_2$ and O$_2$ gases were collected and measured according to the standard H$_2$ and O$_2$ evolution curve by a gas chromatograph.

2.5. DFT Computation part

All reaction energetics were studied by DFT method through the generalized gradient approximation (GGA) with the Perdew-Burke-Ernzerhof (PBE) functional as implemented in Vienna Abinitio Simulation Package (VASP). The monoclinic TiO$_2$ (101) facet models were constructed with a 20 Å vacuum slab in z-direction. A 500 eV cutoff
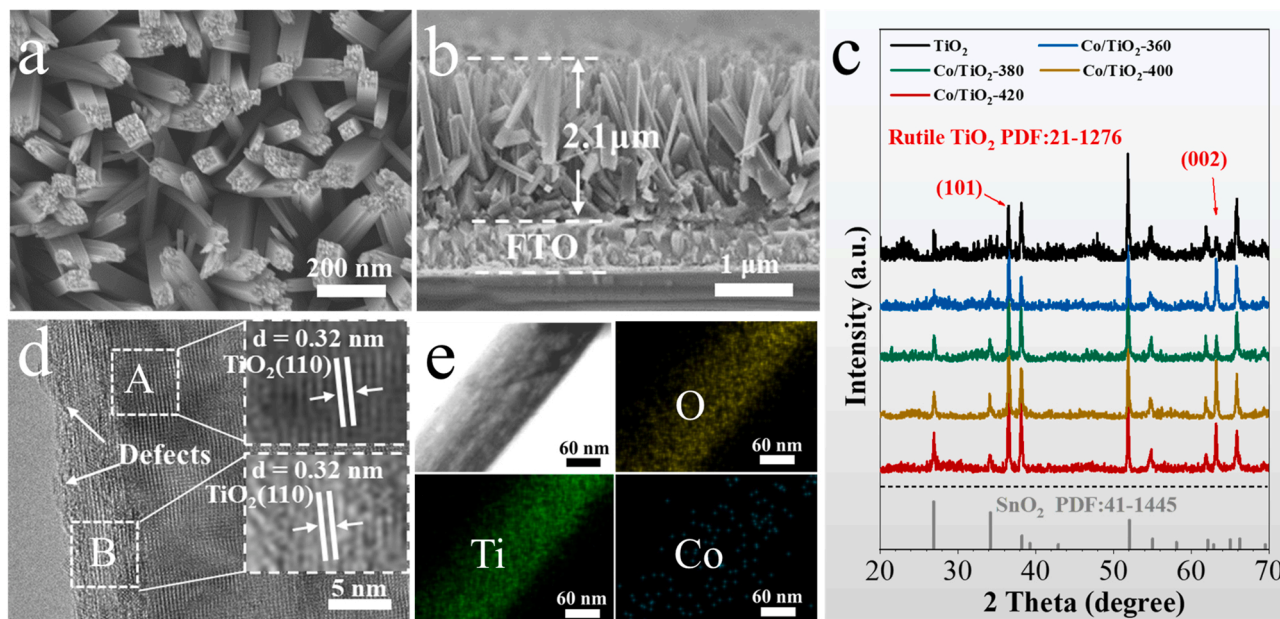
Fig. 1. (a-b) Typical SEM images of Co/TiO$_2$-380 photoanode in different views. (c) Typical XRD patterns of pristine TiO$_2$ and Co/TiO$_2$ sample photoanodes. (d) Typical HRTEM image of Co/TiO$_2$-380 photoanode and the insets are the enlarged images recorded from A and B, respectively. (e) Corresponding elemental mappings of O, Ti and Co within Co/TiO$_2$-380 photoanode.

energy was set for the plane wave. The K-points were set to be $2 \times 2 \times 1$ for (101) surface. All of the calculation models were geometrically optimized until the energy was converged to 1×10^{-5} eV, and all the forces on the free atoms were less than 0.01 eV.Å^{-1}.

Four intermediate states were studied during a OER procedure at the same active site, and Gibbs free energies were obtained based on the thermodynamic energies:

$$\Delta G1 = E(OH) - E_0 + 1/2E(H_2) - E(H_2O) + \Delta ZPE - T\Delta S - eU - k_B T\ln(10) \times pH$$

$$\Delta G2 = E(O) - E(OH) + 1/2E(H_2) - E(H_2O) + \Delta ZPE - T\Delta S - eU - k_B T\ln(10) \times pH$$

$$\Delta G3 = E(OOH) - E(O) + 1/2E(H_2) - E(H_2O) + \Delta ZPE - T\Delta S - eU - k_B T\ln(10) \times pH$$

$$\Delta G4 = E(O_2) - E(OOH) + 1/2E(H_2) - E(H_2O) + \Delta ZPE - T\Delta S - eU - k_B T\ln(10) \times pH$$

where $E(O)$, $E(OH)$, $E(O)$, $E(OOH)$, $E(H_2)$, and $E(H_2O)$ represent the energies of catalyst surface, intermediate products of HO*, O*, HOO*, O$_2$, H$_2$ and H$_2$O, respectively. E was determined from the DFT simulations, while ΔZPE and ΔS (at 298 K) were zero-point vibration energies and entropies retrieved from the literatures, respectively. Actually, all of the Gibbs free energies (ΔG) should be negative, because the free energy decreased during intermediate process. In this work, the overpotential (U) at pH= 0 was only discussed simplicity, which could be calculated by following formula:

$$\eta = \max(\Delta G1, \Delta G2, \Delta G3, \Delta G4)/e - 1.23 \ (V)$$

3. Results and Discussion

3.1. Characterization of photoanodes

Fig. 1(a) is the schematic illustration for constructing TiO$_2$ photoanode with Co SACs. It mainly involves two typical steps, namely, the initial growth of vertically-aligned TiO$_2$ nanowire array on FTO substrate by a hydrothermal method, followed by building Co SACs on the surface of TiO$_2$ nanowires (referred to sample Co/TiO$_2$-T, in which T refers to the reaction temperature) by an *in-situ* gas-phase cation exchange technique (also see Fig. S1, Schematic 1). As shown in Fig. S2(a), the top-view SEM image reveals that the tetragonally shaped nanowire arrays have grown on FTO substrate. After gas-phase cation exchange, no obvious morphology and size changes are observed (Fig. 1(a) and Fig. S2(b-d)). This could be mainly attributed to the similar ionic radius of Co^{2+} (0.072 nm) to that of Ti^{4+} (0.068 nm), as well as a tiny proportion of Ti replaced by Co on the surface of TiO$_2$, which are not enough to cause significant change in structures [46]. Fig. 1(b) presents a typical cross-section SEM image of sample Co/TiO$_2$-380, further confirming the growth of nearly vertical nanowire arrays with a mean length of ~2.1 μm. Fig. 1(c) shows the phase compositions of as-prepared photoanodes. It is observed that all XRD peaks of pristine TiO$_2$ and Co/TiO$_2$ photoanodes respond to the tetragonal rutile phase (JCPDS No.21–1276), in which the dominant ones are assigned to the (101) and (002) planes of rutile TiO$_2$. The enlarged XRD pattern of (101) plane reveal that no obvious peak shift is observed (Fig. S3), suggesting the hardly change in the lattice constants for TiO$_2$. This fact also shows that only tiny Ti has been replaced by Co on the TiO$_2$ surface. The additional signals are attributed to the used FTO substrate, and no distinct peaks of Co-containing species could be observed in all samples, further witnessing that only a small amount of Ti has been replaced. To confirm this point, Raman spectra of pristine TiO$_2$ and Co/TiO$_2$ photoanodes are provided in Fig. S4. Three main Raman peaks are ascribed to the Raman active mode of rutile TiO$_2$ in both samples with no signals for Co-containing species, agreeing on the XRD analyses [45].

Fig. 1(d) is the typical HRTEM image of Co/TiO$_2$-380 sample. The two inset images in Fig. 1(d) are recorded from the inner and outer parts of the marked areas of respective A and B, suggesting that no obvious interface exists, as in the pristine TiO$_2$ nanowires (Fig. S5(a)). The observed fringes distance of 0.32 nm should be indexed to the (110) planes of rutile TiO$_2$ (JCPDS No. 21–1276). It is worth noting that the lattice fringes within the outer part seem a slightly blurred, in comparison to those within inner part, clarifying that the cation exchange reaction between Co^{2+} and Ti^{4+} just occurs on the surface of TiO$_2$. The elemental mapping images (Fig. 1(e)) disclose the uniform spatial distributions of Ti, O and Co within sample Co/TiO$_2$-380. This fact is also
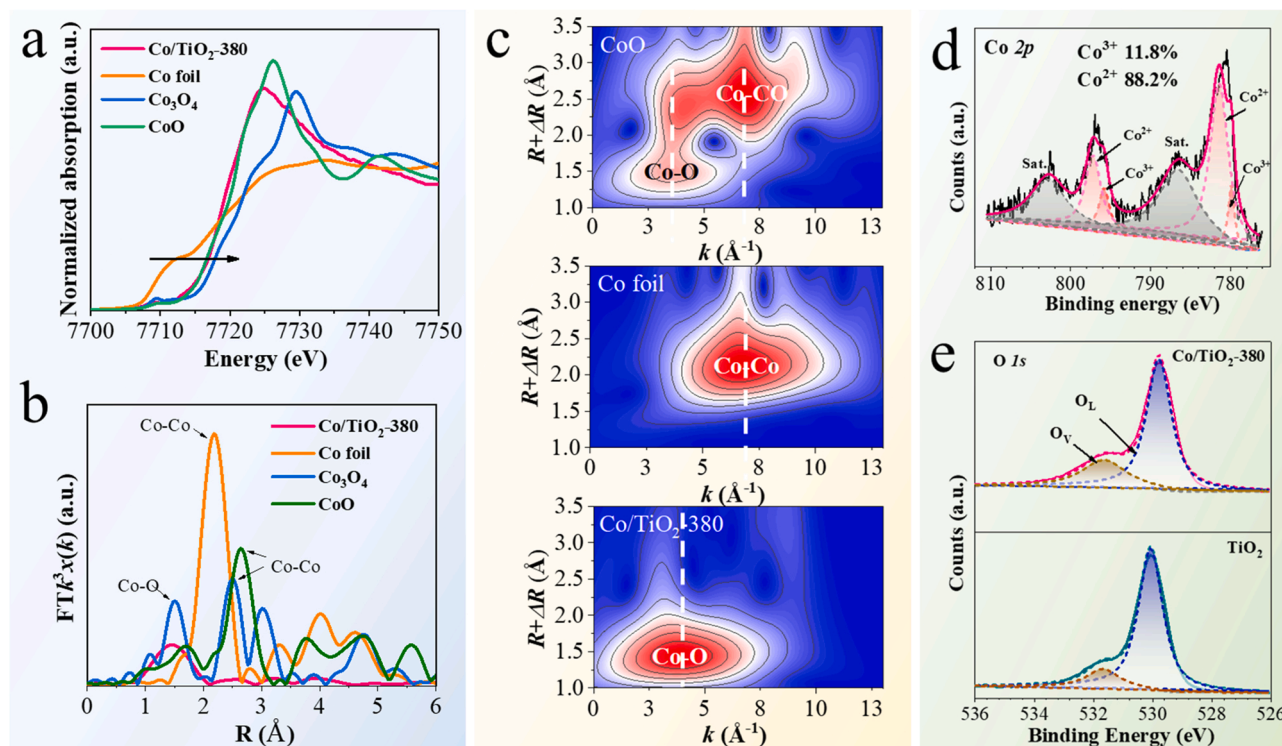
Fig. 2. (a) Co K-edge XANES spectra and (b) Fourier-transformed magnitudes of Co K-edge EXAFS spectra of sample Co/TiO$_2$-380 and comparison counterparts of Co foil, CoO, and Co$_3$O$_4$. (c) Wavelet transforms for k3-weighted EXAFS spectra of CoO, Co foil and Co/TiO$_2$-380. (d-e) High-resolution XPS spectra of Co 2p in Co/TiO$_2$-380, and O 1 s in pristine TiO$_2$ and sample Co/TiO$_2$-380, respectively.

verified by the complete exchange at a higher temperature up to 540 °C with a longer reaction time up to 30 min (Fig. S6).

To monitor the electronic state and coordination environment of Co in Co/TiO$_2$-380 sample, X-ray absorption fine spectroscopy measurements were carried out. Fig. 2(a) presents the Co K-edge X-ray absorption near-edge spectra (XANES) of Co/TiO$_2$-380 sample, revealing that the absorption edge of Co is closed to that of CoO, and different to those of Co foil and commercial Co$_3$O$_4$. Thereby, it implies that the oxidation state of Co species in Co/TiO$_2$-380 sample is closer to divalent, and the bonding is achieved through Co-O electronic coupling [47]. The extended EXAFS is also recorded at Co K edge to disclose the local coordination environment of Co species [48]. Fig. 2(b) shows the R space transformation pattern, in which a strong peak at 1.46 Å is assigned to the Co-O bonds. No characteristic peaks of Co-Co and Co-O-Co can be detected. Thus, this fact can exclude the Co-Co interaction within sample Co/TiO$_2$-380 and the existence of Co/CoO$_x$ species, which confirm the separation and coordination of Co atoms with surrounding O atoms in TiO$_2$. The coordination range of atomically-dispersed centers is then quantified by least squares EXAFS curve fitting analysis (Fig. S7 and Table S1). The fitting results demonstrate that the Co-O bond length in sample Co/TiO$_2$-380 is 2.01 Å, different to that of Co-Co bond length (2.49 Å) in Co foil. In addition, the further quantitative EXAFS curve fitting analyses show that Co/TiO$_2$-380 sample has an estimated Co-O bond coordination number of 6.2 in the first coordination spheres, consistent with that of Ti-O coordination in TiO$_2$ [47], implying that the displaced Co sites form a configuration similar to that of Ti in TiO$_2$. The wavelet transform (WT) simulations were also performed to analyze the radial distance resolution in K-space. As shown in Fig. 2(c) and Fig. S8, the WT intensity maxima resulting from Co-O coordination near 4.0 Å^{-1} are well resolved at 1.0–2.0 Å with no Co-Co coordination in Co/TiO$_2$-380 sample, reflecting that the Co atoms are dispersed separately with Co-O coordinated sites. It should be pointed that the temperature of thee gas-phase cation exchange reaction greatly affects formation of Co single-atom site on the TiO$_2$ surface because the

substitution reaction ratio and reaction rate should be precisely controlled. The HRTEM images of the samples prepared at 400 °C (Co/TiO$_2$-400) and 420 °C (Co/TiO$_2$-420) show that some tiny CoO clusters were formed on the TiO$_2$ surface (Fig. S9). Thus, it is confirmed that the formation of Co single-atom site in TiO$_2$ only when the gas-phase cation exchange reaction was carried out at a relatively low temperature.

X-ray photoelectron spectroscopy (XPS) was also utilized to further study the elemental states of Co/TiO$_2$-380 sample. The high-resolution XPS spectra of Co 2p indicate the existence of two valence states (*i.e.,* +2 and +3) for Co element (Fig. 2(d)). Based on the quantitative analysis, the Co^{2+} valence accounts for 88.2% (Table S2), which indicates that the valence of Co is close to + 2, agreeing on the XANES results as mentioned above. As for the high-resolution XPS spectra of O 1 s recorded from pristine TiO$_2$ and Co/TiO$_2$-380 sample (Fig. 2(e)), both of them can be deconvoluted into two peaks associated with the lattice O (O$_L$) and oxygen vacancies (O$_V$) [35]. It should be pointed out that Co/TiO$_2$-380 sample possesses a higher O$_V$ proportion (21.71%) than that of pristine TiO$_2$ (17.3%) (Table S3). Accordingly, it is confirmed that the incorporated Co SAC into TiO$_2$ can increase the surface defect, consistence with the HRTEM characterization. Fig. S10 shows the high-resolution XPS spectra of Ti 2p for pristine TiO$_2$ and sample Co/TiO$_2$-380. As compared to the pristine TiO$_2$, Co/TiO$_2$-380 sample exhibits a negative shift in terms of the binding energies in Ti 2p XPS spectra, verifying the decreased valence state of surface Ti. This is because the incorporated Co with lower valence enables fewer electron loss of surface Ti, implying the significant influence on the electronic structure nearby Ti [20].

3.2. PEC performance testing

The PEC water oxidation performances over as-prepared photoanodes are evaluated in 1 M KOH electrolyte under simulated sunlight irradiation (AM 1.5 G, 100 mW cm^{-2}). Fig. S11 displays the linear
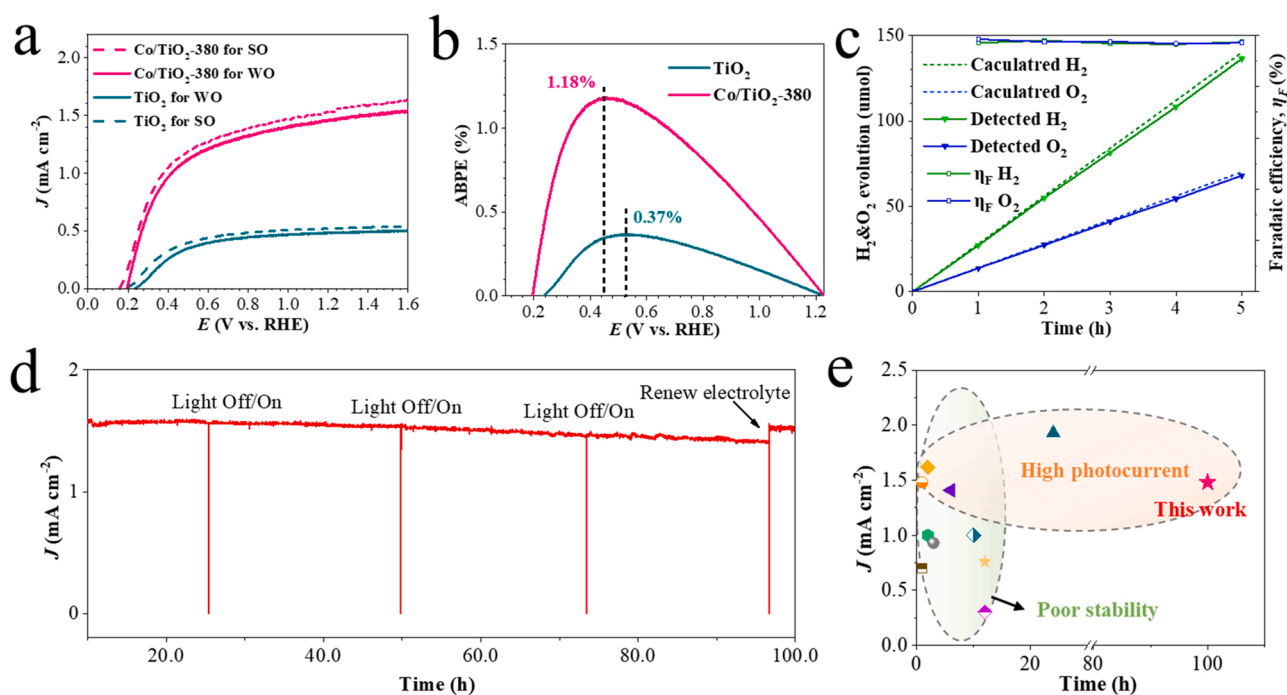
Fig. 3. (a-b) *J-V* curves and applied bias photon-to-current efficiency (ABPE) of pristine TiO$_2$ and sample Co$_2$/TiO$_2$-380, respectively. (c) The gas evolutions and Faradaic efficiencies of pristine TiO$_2$ and sample Co$_2$/TiO$_2$-380 under RHE 1.23 V. (d) Long-term stability over Co/TiO$_2$-380 photoanode. (e) The comparison of PEC performance with some representatively reported TiO$_2$-based photoanodes.

sweep voltammetry (LSV) curves under chopping irradiation condition, showing that the photocurrent does not appear under dark. It seems that the pristine TiO$_2$ photoanode only presents a relatively low photocurrent density of 0.48 mA cm^{-2} at 1.23 V *vs.* RHE. For comparison, all Co/TiO$_2$ analogues exhibit fundamentally increased photocurrent densities, clarifying that the atomically-dispersed Co sites effectively enhance the PEC activity of TiO$_2$ photoanodes. The PEC activity remarkably depends on the fixed reaction temperatures, and becomes reduced as the temperature rises to 400 °C. This could be mainly due to the fact that the introduced Co sites with high amount enough would also create new charge recombination sites, thus causing a reduced PEC performance. The optimal one based on Co/TiO$_2$-380 sample presents a photocurrent density of 1.47 mA cm^{-2} at 1.23 V *vs.* RHE, which is ~3.1 times to that of pristine TiO$_2$ (*i.e.,* 0.48 mA cm^{-2}). Furthermore, its onset potential (*V$_{Onset}$*) behaves a significant negative shift as compared to that of pristine TiO$_2$, reaching 0.18 V *vs.* RHE. It suggests that the atomically-dispersed Co can reduce the OER barriers effectively, responsible for the negative shift of onset potential. To disclose the contribution of oxygen vacancies on PEC behaviors, the TiO$_2$-O$_V$ photoanodes were prepared under the identical temperature for tailoring the oxygen vacancies (Fig. S12(a-b)), of which the details are provided in Supporting Information. The PEC test reveals that its photocurrent density is up to 0.76 mA cm^{-2} at 1.23 V *vs.* RHE (Fig. S12(c-d)), which is higher than that of pristine TiO$_2$ but still much lower than that of Co/TiO$_2$-380 (*i.e.,* 1.47 mA cm^{-2}). These results indicate that the introduced oxygen vacancies contribute to the PEC performance improvement, whereas the atomically-dispersed Co in Co/TiO$_2$ photoanode still plays the dominant role.

Fig. 3(b) provides the applied bias photon current efficiency (ABPE) of the photoanodes based on pristine TiO$_2$ and Co/TiO$_2$-380 sample. It reveals that a maximum ABPE value of 1.18% can be achieved for Co/TiO$_2$-380 sample at a low bias of 0.45 V (*vs.* RHE), while that of pristine TiO$_2$ is only 0.37% even at a relatively higher bias of 0.53 V (*vs.* RHE). The corresponding H$_2$ and O$_2$ evolutions over Co/TiO$_2$-380 photoanode were also tested by an online gas chromatography (GC). As shown in Fig. 3(c), the produced H$_2$ and O$_2$ amounts are close to the theoretical

ones over 5 h reaction, with a Faradaic efficiency (FE) more than 97% for water splitting. Fig. S13 presents the PEC tests under switched condition of light on/off. It seems that the overall photocurrent of the photoanodes based on pristine TiO$_2$ and Co/TiO$_2$-380 sample hardly decay over time, whereas that over Co/TiO$_2$-380 sample is much higher than that of pristine TiO$_2$ at the moment of light on, reflecting the significantly enhanced charge transfer. Fig. 3(d) and Fig. S14 reveal that the photocurrent of Co/TiO$_2$-380 sample exhibits only a 4.1% drop over 100 h at a fixed bias of 1.23 V (*vs.* RHE), suggesting the excellent stability. This slight decline of photocurrent might come from the loss of electrolyte, since the performance can return to its original state by supplementing the electrolyte. The microstructure and chemical state of the Co/TiO$_2$-380 photoanode after long-term stability testing were further studied by SEM and XPS, respectively. No obvious morphology changes are observed (Fig. S15(a)), showing the excellent stability of as-constructed photoanode. The deconvolution of the Co 2p XPS spectrum shown in Fig. S15(b) reveal that the Co^{2+} is still the dominant chemical state of the Co atom while the decreased proportion of Co^{2+} can be attributed to the slight oxidation during the long-term water oxidation reaction. Also, the formation of single-atom site of Co on the TiO$_2$ surface in a Ti coordination environment of the as-prepared photoanode, which make it not easy to electrochemically dissolve into the solution, leading to the high stability during long-term tests. Furthermore, the Co ions concentration of the electrolyte at different test times during the long-term experiment were measured by using ICP-MS. The results (Table S4) show that a certain proportion of Co was dissolved into the electrolyte during long-term test reaction. However, it is noted that the dissolved amount of Co did not increase significantly as the test time prolong. The slight dissolved Co mainly comes from the small amount of non-substituted Co components on the surface of TiO$_2$ while the internal Co that incorporated in the TiO$_2$ lattice still has higher stability. Thus, it is not easy to cause a large amount of dissolution of Co during long-term experiment. To further study the stability, the PEC tests of Co/TiO$_2$-380 sample photoanode have conducted in acidic (0.5 M H$_2$SO$_4$) and neutral (0.5 M Na$_2$SO$_4$) pH conditions. The results show that the sample photoanode still display excellent stability both at neutral or acidic pH
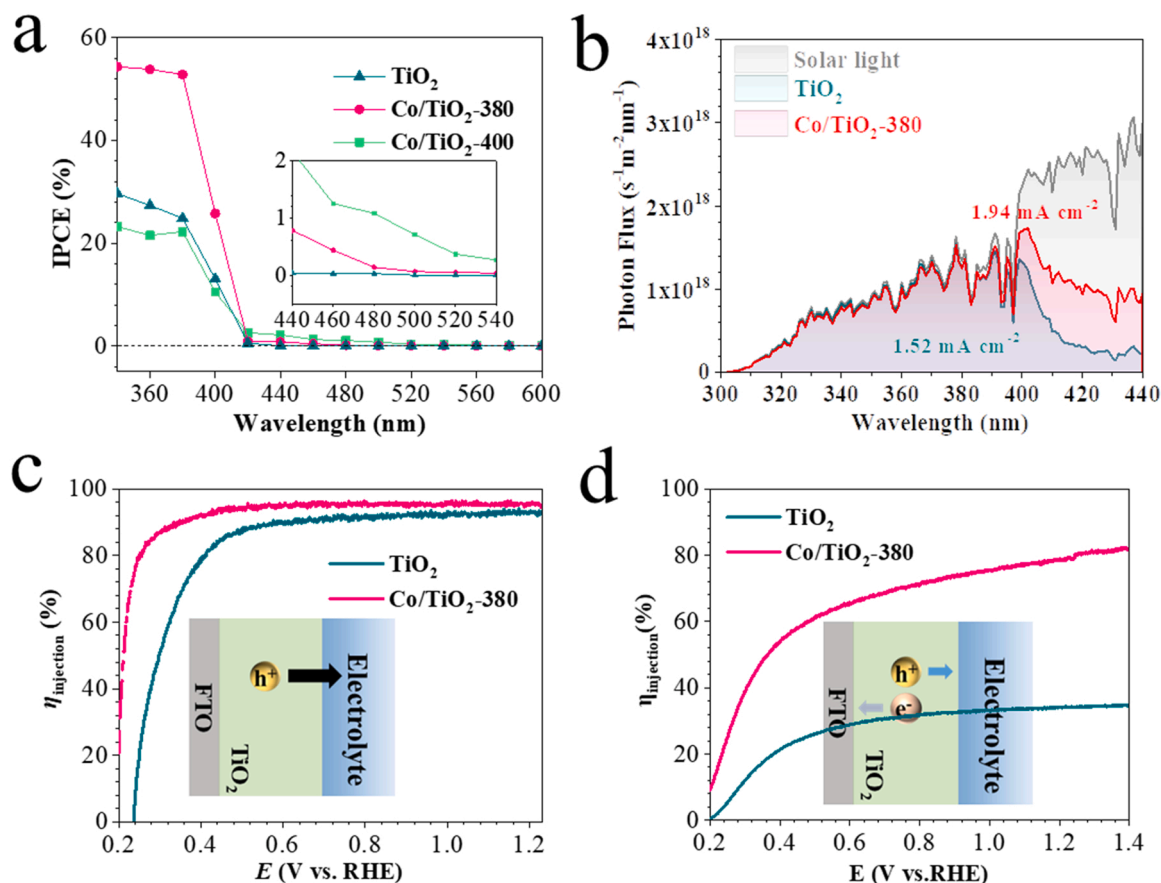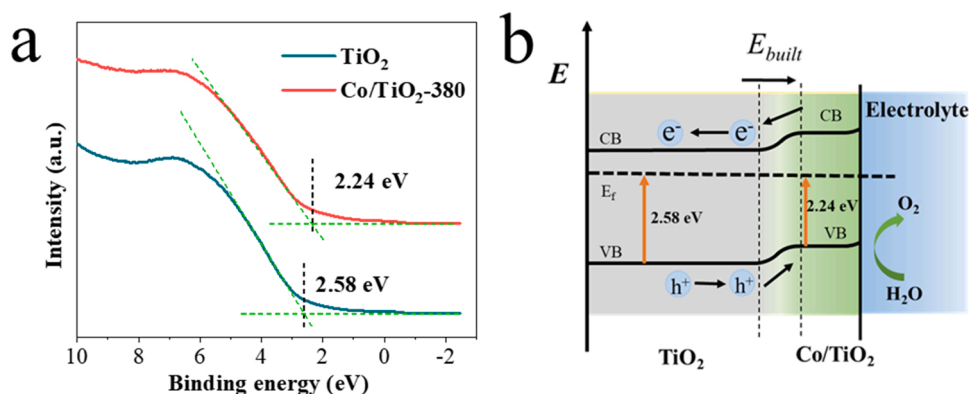
Fig. 4. (a) IPCE of pristine TiO$_2$, sample Co/TiO$_2$-380 and Co/TiO$_2$-400 at 1.23 V *vs.* RHE. (b) Standard AM 1.5 G solar spectrum and theoretical absorption spectra of photoanodes. (c-d) The surface charge separation and separation efficiencies of pristine TiO$_2$ and sample Co/TiO$_2$-380, respectively.

conditions (Fig. S16(a-d)). However, it is worth noting that the achieved photocurrent density is slightly lower than that in alkaline condition, suggesting that the alkaline environment is better than the neutral and acidic environment for water oxidation reaction. More interestingly, it is noticeable that the achieved photocurrent density (Fig. 3(e)) and stability of our Co/TiO$_2$-380 photoanode in alkaline electrolyte are higher than those of most TiO$_2$-based photoanodes ever reported (Table S5), representing the boosted PEC performance of TiO$_2$ photoanodes induced by atomically-dispersed Co.

3.3. Mechanism analysis of PEC

Fig. 4(a) shows the incident-photon-to-current conversion efficiencies (IPCE) of the photoanodes based on pristine TiO$_2$, Co/TiO$_2$-380 and Co/TiO$_2$-400 samples at 1.23 V (*vs.* RHE). It evidences that the IPCE of sample Co/TiO$_2$-380 is much higher than those of pristine TiO$_2$ and Co/TiO$_2$-400 samples in the ultraviolet range from 340 to 400 nm. Particularly, the maximal IPCE is up to 54% at 340 nm, which is ~1.7 time to that of pristine TiO$_2$. The inset in Fig. 4(a) provides the enlarged IPCE plots at visible-light region, suggesting that the Co/TiO$_2$-based photoanodes deliver much higher IPCE than that of pristine TiO$_2$ with negligible one. This implies that the atomically-dispersed Co on the surface of TiO$_2$ could broaden the light response range. To verify this point, their UV−vis absorption spectra are collected correspondingly. It demonstrates that the Co/TiO$_2$-based photoanodes behave an obvious red shift with improved absorption in the range of 400–600 nm, in

Fig. 5. (a) UPS characterizations of pristine TiO$_2$ and Co/TiO$_2$-380 samples. (b) The corresponding energy band schematic diagram.
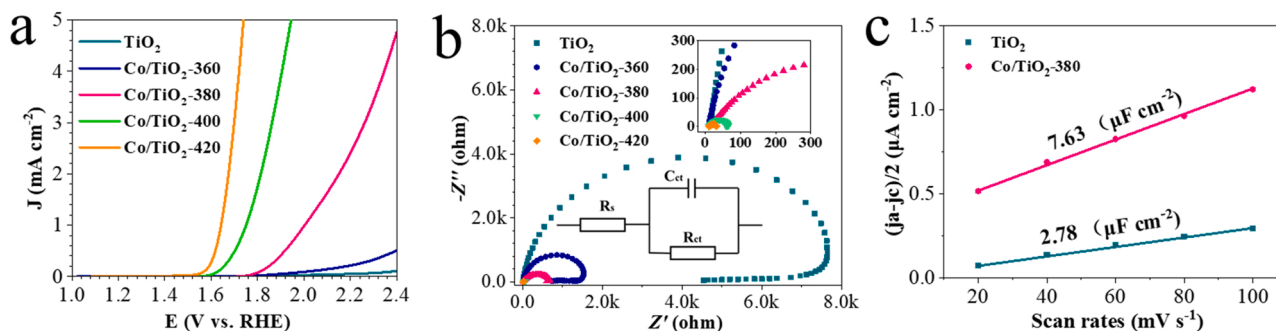
Fig. 6. LSV curves (a), EIS curves (b) and electrochemical active areas (c) for pristine TiO_2 and Co/TiO_2 sample photoanodes in dark.

comparison to that of pristine TiO_2 (Fig. S17(a)). Based on the Kubelka-Munk function (Fig. S17(b)), the calculated bandgaps are reduced from 3.05 eV of pristine TiO_2 to 3.01 eV of Co/TiO_2-380 sample. Accordingly, by integrating the UV−vis absorption spectra with the standard solar spectrum of AM 1.5 G (Fig. 4(b) and Fig. S17(a-b)), Co/TiO_2-380 sample exhibits a higher photocurrent density of 1.94 mA cm^{-2}, much higher than that of pristine TiO_2 (i.e., 1.52 mA cm^{-2}). The surface charge injection efficiencies ($\eta_{injection}$) and bulk charge separation efficiencies ($\eta_{seperation}$) of the photoanodes were studied by a hole-scavenger-assisted PEC measurement. As shown in Fig. 4(c), the $\eta_{injection}$ of pristine TiO_2 and sample Co/TiO_2-380 can be calculated from $J_{H2O}/J_{sulfite}$, where J_{H2O} and $J_{sulfite}$ are the photocurrent densities achieved by the oxidation of H_2O and Na_2SO_3, respectively. As compared to pristine TiO_2, the Co/TiO_2-380 photoanode presents improved $\eta_{injection}$ in low-bias region with no significant difference at high-bias region (both of them are ~94% at 1.23 V vs. RHE), implying that the surface charge injection should not be the main reason for boosting the PEC performance. However, the $\eta_{seperation}$ values of pristine TiO_2 and sample Co/TiO_2-380 are ca. 33.5% and 78.7% at 1.23 vs. RHE, verifying the significantly enhanced charge separation by the atomically-dispersed Co.

To clarify the above point, the changes of electronic structure and band edges are further studied by valence band (VB) XPS spectroscopy. As disclosed in Fig. 5(a), Co/TiO_2-380 sample presents a shift of 0.34 eV in VB edge, as compared to that of pristine TiO_2. Considering the little difference of band gap between sample Co/TiO_2-380 and pristine TiO_2 (Fig. S15(b)), the conduction band (CB) edge will experience an almost identical shift as VB edge does, mainly attributed to the substitution of surface Co and the introduction of O_L. Consequently, the elevated band edge enables the formation of a type-II homojunction within the Co/TiO_2 photoanode, thus creating a built-in electric field to promote the holes migrated to the surface. Furthermore, the surface photovoltage (SPV) technique was employed to investigate the separation and transfer behaviors of photogenerated carriers. As shown in Fig. S18, the largely increased SPV signal intensity of Co/TiO_2-based photoanode indicates an improved capacity for holes transport [26]. Fig. 5(b) proposes a possible charge separation mechanism for Co/TiO_2 photoanode. As for pristine TiO_2, it often has insufficient charge-separation ability, due to

the fast recombination of photo-generated carriers. Once the atomically-dispersed of Co is introduced on the surface of TiO_2, the near-surface band edge would be elevated for constructing a typical type-II junctions between Co/TiO_2 and TiO_2, providing a direct driving force for charge separation and migration. In such case, the photo-generated holes are expected to transfer from the VB of TiO_2 to that of Co/TiO_2, while the electrons will transfer in an opposite way from the CB of Co/TiO_2 to that of TiO_2 separately, thereby promoting the redox reactions on the surface.

3.4. Mechanism analysis of water oxidation activity

To understand the oxygen evolution reaction (OER) activity, the LSV curves of these samples were measured under dark conditions (Fig. 6 (a)). It suggests that the Co/TiO_2 samples possess much lower over-potentials and higher water oxidation currents than pristine TiO_2, witnessing the fundamentally enhanced OER activity. When higher concentration of Co is incorporated, the OER activity is gradually increased, confirming that the atomically-dispersed Co should be serviced as the active sites to facilitate the surface reactions. In addition, the electrochemical impedance spectroscopy (EIS) was also tested in dark to elucidate the electron transfer resistance at the photoanode/electrolyte interface, which includes series resistance (R_s), charge transfer resistance (R_{ct}), and constant phase angle element (CPE) (Fig. 6 (b)). The corresponding fitting resistances (Table S6) reveal that the Rct values are decreased dramatically from 6429 to 51.33 Ω with the increase of introduced Co in TiO_2, illustrating the significantly enhanced interfacial charge transfer at photoelectrode-electrolyte interface. Moreover, the electrochemical double-layer capacitance (C_{dl}) was also examined to evaluate the electrochemically active surface area (ECSA) by cyclic voltammetry (CV) at different scan rates in non-Faradaic region (Fig. S19). The slopes calculated from CV plots are shown in Fig. 6 (c), suggesting that the ECSA values of sample Co/TiO_2-380 and pristine TiO_2 are 7.63 and 2.78 μF cm^{-2}, respectively. This result further proves that the atomically-dispersed of Co on TiO_2 increases the specific surface area and enriches the active site, thus leading to an improved OER activity [49].(Scheme 1).
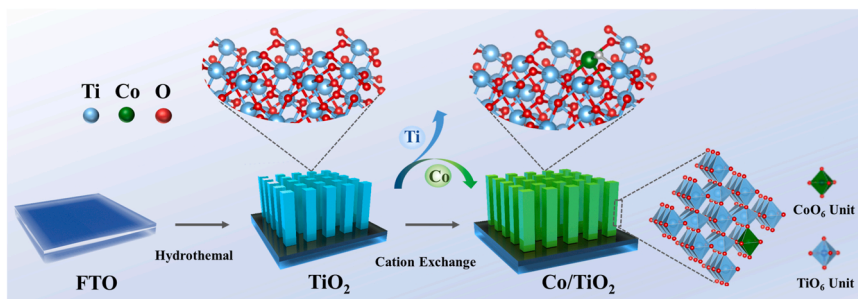
Scheme 1. Diagram of the preparation process for Co/TiO_2 photoanode.
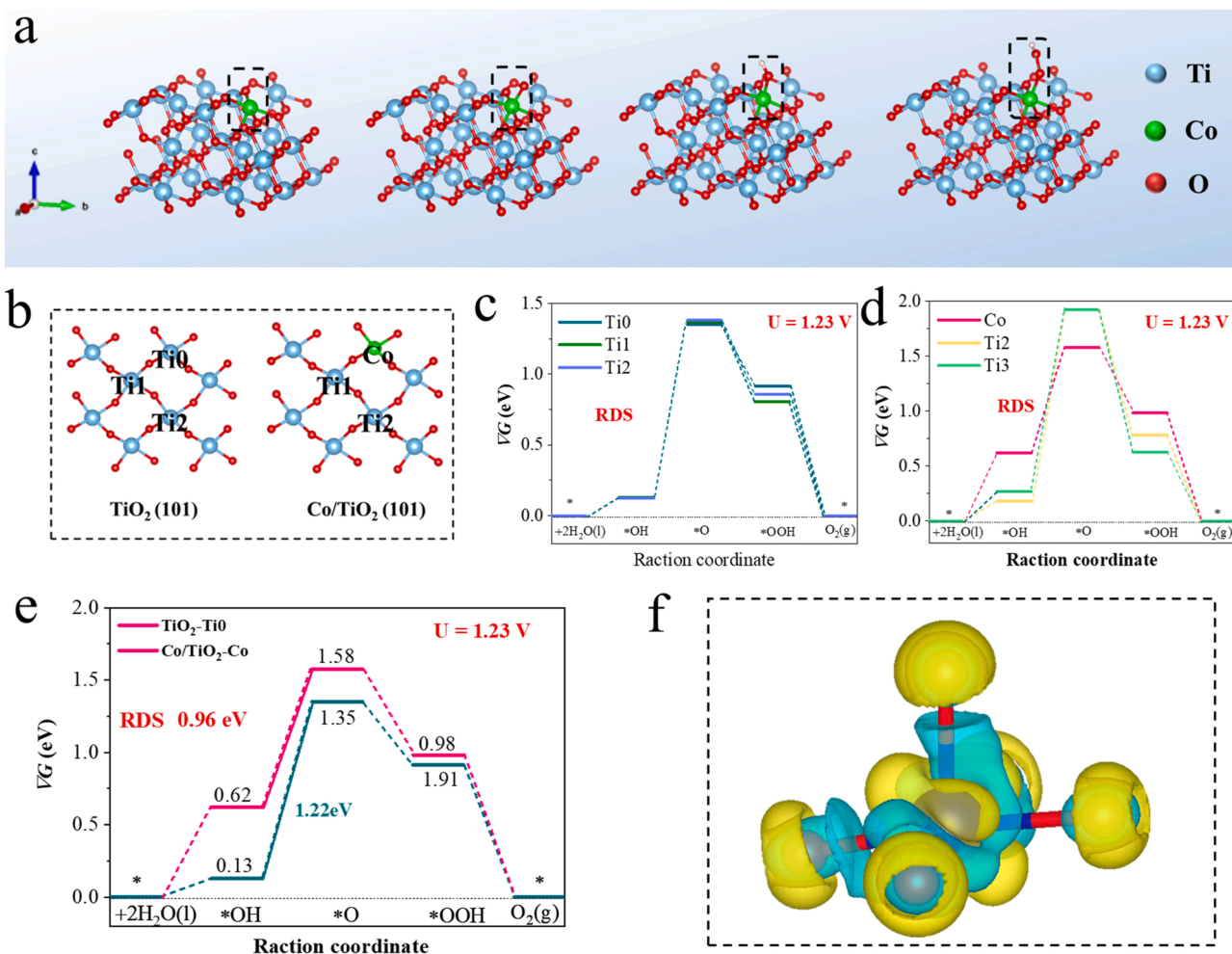
Fig. 7. (a) Molecular structure models for DFT Calculations. From left to right is the slabs and the adsorption models of O, OH, OOH, where the adsorption site is Co. (b) Schematic diagrams of adsorption sites for Gibbs free energy calculations based on the models of pristine TiO_2 and sample Co/TiO_2. (c) Gibbs free energy diagrams for water oxidation reaction intermediates over the sites of Ti0, Ti1 and Ti2 of pristine TiO_2 (d) Gibbs free energy diagrams for water oxidation reaction intermediates over the sites of Co, Ti1 and Ti2 on sample Co/TiO_2 (e) Gibbs free energy diagrams for water oxidation reaction intermediates over the sites of Ti0 on pristine TiO_2 and Co on sample Co/TiO_2. (f) Differential charge map of Co sites for molecular models of Co/TiO_2. The yellow and blue colors indicate the electron accumulation and depletion, respectively.

The DFT calculations were conducted to reveal the origin of better OER behaviors. In general, the overall water oxidation of OER can divided into four basic steps, in respect to the formation of *OH, *O and *OOH and *O_2 intermediates. In such cases, the energy barrier is related to the Gibbs free energy change (ΔG), of which the maximum one is regarded as a rate-determining step (RDS) [50]. The (101) crystal plane of TiO_2 is used as the basic atomic structure model for the calculation, and part of Ti on the surface is replaced by Co as the Co/TiO_2 model (Fig. S20). Fig. 7(a) shows the slabs and the adsorption models of O, OH, OOH, where the adsorption site is Co, respectively, of the Co/TiO_2 sample. As shown in Fig. 7(b), the Ti site in the surface of $TiO_2(101)$ were selected as the adsorption site. According to the symmetry, three sites were selected to represent all the Ti sites in the surface, named Ti0, Ti2 and Ti3, respectively. Similarly, Co is used instead of Ti0 site in the $Co/TiO_2(101)$ model, and the selection of Ti2 and Ti3 sites is consistent with that of $TiO_2(101)$ (Fig. 7(b)).

As shown in Fig. 7(c) and Fig. S21, for pristine TiO_2, it is observed that the Gibbs free energy profiles for OER are almost overlapped at three different sites (U = 1.23 V). This suggests the equivalent calculations for each Ti site on the surface of pristine TiO_2, demonstrating that replacing the Ti0 site with Co is accurate and representative for further analyses. Additionally, it means that the electrochemical step from *OH to *O can be regarded as the RDS, which delivers a highest overpotential

(η) of 1.22 eV for pristine TiO_2. After the replacement of Ti0 site by Co, it is found that the entire reaction path on Co sites is much smaller as compared to those of Ti2 and Ti3 sites in Co/TiO_2 model (Fig. 7(d), Fig. S22), indicating a reduced energy barrier for OER reaction. According to the calculation results, the conversion of *OH to *O should be the RDS for Co/TiO_2. Moreover, the flattened ΔG profile suggests that the Co sites on Co/TiO_2 are more suitable for realizing water oxidation with a small overpotential. To further compare the energy barriers, the Gibbs free energy profiles of Ti and Co site in pristine TiO_2 and sample Co/TO_2 are provided in Fig. 7(e), respectively (U = 1.23 V). Obviously, the energy barrier (η) of sample Co/TiO_2 with the RDS for the transition from *OH to *O is substantially decreased to 0.96 eV, in comparison to that of pristine TiO_2, verifying that the introduced Co atoms accelerate the reaction kinetics for PEC water oxidation. Furthermore, Fig. 7(e) displays the optimized model for the adsorption of reaction intermediates, showing that the second step from *OH to *O should be the potential RDS. The different electron densities illustrate that the electrons tend to accumulate around the Co atom (Fig. 7(f) and Fig. S23). Consequently, these localized electrons are expected to be transferred into the antibonding orbitals of water molecules for water activation, underscoring that the atomically-dispersed Co could reduce the free energy barriers to accelerate the reaction kinetics toward boosted PEC behaviors. To explore the origin of the enhanced PEC performance,
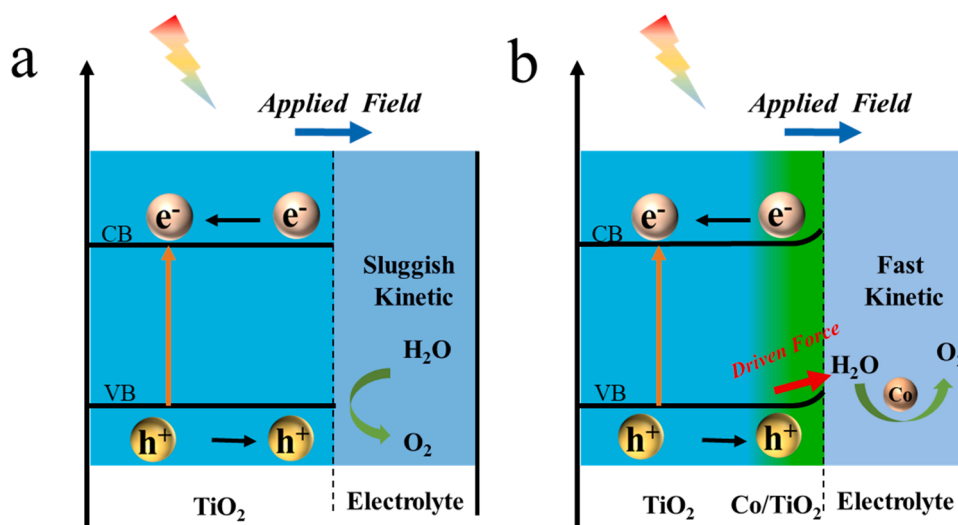
Scheme 2. (a-b) Schematic diagram of pristine TiO_2 (a) and Co/TiO_2 (b) photoanode for OER reaction, respectively.

schematic diagrams of the charge transfer process of TiO_2 and Co/TiO_2 photoanodes are shown in Scheme 2(a-b). The low PEC performance of the pristine TiO_2 photoanodes is attributed to the slow water oxidation kinetics and slow charge transfer kinetics. In contrast, the surface band modulation of Co/TiO_2 effectively improves the hole transport ability and the Co sites enhance the OEC activity together to achieve superior PEC activity.

4. Conclusion

In conclusion, we have demonstrated a facile strategy based on *in-situ* gas-phase cation exchange of Ti^{4+} by Co^{2+} for engineering single-atomic Co on the surface of TiO_2 photoanode toward efficient and durable solar water splitting. The EXAFS and XANES analyses confirm that atomically-dispersed Co sites have been built on the surface of TiO_2 enabled by the Co-O bonds. The as-fabricated Co/TiO_2 photoanode delivers a high photocurrent density of 1.47 mA cm^{-2} at 1.23 V *vs.* RHE and long-term durability under AM 1.5 G illumination, surpassing those of pristine TiO_2 and most TiO_2-based counterparts ever reported. The experimental and theory calculations disclose that the introduced Co SACs could optimize the surface electronic structures, expand the light absorption range, facilitate the holes transfer, lower the free energy barriers and accelerate the reaction kinetics, which thus favor the boosted PEC performance of TiO_2 photoanodes. The present work might provide some insight on rationally designed SACs for exploring advanced photoanodes toward efficiency and durable PEC water oxidation.

CRediT authorship contribution statement

Kai Song: Investigation, Formal analysis, Writing – original draft. **Huilin Hou:** Methodology, Supervision, Funding acquisition, Writing – review & editing. **Dongdong Zhang:** Formal analysis. **Fang He:** Conceptualization, Supervision, Funding acquisition. **Weiyou Yang:** Supervision, Funding acquisition, Writing – review & editing.

Declaration of Competing Interest

The authors declare that they have no known competing financial interests or personal relationships that could have appeared to influence the work reported in this paper.

Data Availability

Data will be made available on request.

Appendix A. Supporting information

Supplementary data associated with this article can be found in the online version at doi:10.1016/j.apcatb.2023.122630.

References

[1] R.-T. Gao, X. Guo, S. Liu, X. Zhang, X. Liu, Y. Su, L. Wang, Ultrastable and high-performance seawater-based photoelectrolysis system for solar hydrogen generation, Appl. Catal. B-Eviron. 304 (2022), 120883, https://doi.org/10.1016/j.apcatb.2021.120883.

[2] C.B. Bie, L.X. Wang, J.G. Yu, Challenges for photocatalytic overall water splitting, Chem 8 (2022) 1567–1574, https://doi.org/10.1016/j.chempr.2022.04.013.

[3] M. Yu, E. Budiyanto, H. Tuysuz, Principles of water electrolysis and recent progress in cobalt-, nickel-, and iron-based oxides for the oxygen evolution reaction, Angew. Chem. Int. Ed. 61 (2022), e202103824, https://doi.org/10.1002/anie.202103824.

[4] X. Liu, J. Meng, J. Zhu, M. Huang, B. Wen, R. Guo, L. Mai, Comprehensive understandings into complete reconstruction of precatalysts: synthesis, applications, and characterizations, Adv. Mater. 33 (2021), e2007344, https://doi.org/10.1002/adma.202007344.

[5] J. Yin, J. Jin, H. Lin, Z. Yin, J. Li, M. Lu, L. Guo, P. Xi, Y. Tang, C.H. Yan, Optimized metal chalcogenides for boosting water splitting, Adv. Sci. 7 (2020) 1903070, https://doi.org/10.1002/advs.201903070.

[6] Y. Xue, Y. Wang, Z. Pan, K. Sayama, Electrochemical and photoelectrochemical water oxidation for hydrogen peroxide production, Angew. Chem. Int. Ed. 60 (2021) 10469–10480, https://doi.org/10.1002/anie.202011215.

[7] D.M. Zhao, Y.Q. Wang, C.L. Dong, Y.C. Huang, J. Chen, F. Xue, S.H. Shen, L.J. Guo, Boron-doped nitrogen-deficient carbon nitride-based Z-scheme heterostructures for photocatalytic overall water splitting, Nat. Energy 6 (2021) 388–397, 10.1038/s41560-021-00795-9.

[8] X. Li, Y. Chen, Y. Tao, L. Shen, Z. Xu, Z. Bian, H. Li, Challenges of photocatalysis and their coping strategies, Chem. Catal. 2 (2022) 1315–1345, https://doi.org/10.1016/j.checat.2022.04.007.

[9] E. Zhao, K. Du, P.F. Yin, J. Ran, J. Mao, T. Ling, S.Z. Qiao, Advancing photoelectrochemical energy conversion through atomic design of catalysts, Adv. Sci. 9 (2022), e2104363, https://doi.org/10.1002/advs.202104363.

[10] B. He, S. Jia, M. Zhao, Y. Wang, T. Chen, S. Zhao, Z. Li, Z. Lin, Y. Zhao, X. Liu, General and robust photothermal-heating-enabled high-efficiency photoelectrochemical water splitting, Adv. Mater. 33 (2021) 2004406, https://doi.org/10.1002/adma.202004406.

[11] W. Li, Z. Wei, K. Zhu, W. Wei, J. Yang, J. Jing, D.L. Phillips, Y. Zhu, Nitrogen-defect induced trap states steering electron-hole migration in graphite carbon nitride, Appl. Catal. B-Eviron. 306 (2022), 121142, https://doi.org/10.1016/j. apcatb.2022.121142.

[12] P. Christopher, S. Jin, K. Sivula, P.V. Kamat, Why seeing is not always believing: common pitfalls in photocatalysis and electrocatalysis, ACS Energy Lett. 6 (2021) 707–709, https://doi.org/10.1021/acsenergylett.1c00064.

[13] Q. Wang, K. Domen, Particulate photocatalysts for light-driven water splitting: mechanisms, challenges, and design strategies, Chem. Rev. 120 (2020) 919–985, https://doi.org/10.1021/acs.chemrev.9b00201.

[14] S. Lin, H. Huang, T. Ma, Y. Zhang, Photocatalytic oxygen evolution from water splitting, Adv. Sci. 8 (2020) 2002458, https://doi.org/10.1002/advs.202002458.

[15] S.M. Thalluri, L. Bai, C. Lv, Z. Huang, X. Hu, L. Liu, Strategies for semiconductor/ electrocatalyst coupling toward solar-driven water splitting, Adv. Sci. 7 (2020) 1902102, https://doi.org/10.1002/advs.201902102.

[16] J.R. Hemmerling, A. Mathur, S. Linic, Design principles for efficient and stable water splitting photoelectrocatalysts, Acc. Chem. Res. 54 (2021) 1992–2002, https://doi.org/10.1021/acs.accounts.1c00072.

[17] A. Govind Rajan, J.M.P. Martirez, E.A. Carter, Why do we use the materials and operating conditions we use for heterogeneous (Photo)electrochemical water splitting, ACS Catal. 10 (2020) 11177–11234, https://doi.org/10.1021/ acscatal.0c01862.

[18] A. Fujishima, K. Honda, Electrochemical photolysis of water at a semiconductor electrode, Nature 238 (1972) 37–38, https://doi.org/10.1038/238037a0.

[19] T.S. Zhou, L. Li, J.H. Li, J.C. Wang, J. Bai, L.G. Xia, Q.J. Xu, B.X. Zhou, Electrochemically reduced TiO2 photoanode coupled with oxygen vacancy-rich carbon quantum dots for synergistically improving photoelectrochemical performance, Chem. Eng. J. 425 (2021), 131770, https://doi.org/10.1016/j. cej.2021.131770.

[20] W. Ma, K. Huang, X. Wu, M. Wang, S. Feng, Surface polarization enables high charge separation in TiO2 nanorod photoanode, Nano Res. (2021) 4056–4062, https://doi.org/10.1007/s12274-021-3340-0.

[21] P. Zhang, X.F. Lu, D. Luan, X.W. Lou, Fabrication of heterostructured Fe2TiO5–TiO2 nanocages with enhanced photoelectrochemical performance for solar energy conversion, Angew. Chem. Int. Ed. 132 (2020) 8205–8209, https://doi.org/ 10.1002/ange.202000697.

[22] P. Wen, F. Su, H. Li, Y. Sun, Z. Liang, W. Liang, J. Zhang, W. Qin, S.M. Geyer, Y. Qiu, L. Jiang, A Ni2P nanocrystal cocatalyst enhanced TiO2 photoanode towards highly efficient photoelectrochemical water splitting, Chem. Eng. J. 385 (2020), 123878, https://doi.org/10.1016/j.cej.2019.123878.

[23] P. Yue, H. She, L. Zhang, B. Niu, R. Lian, J. Huang, L. Wang, Q. Wang, Super-hydrophilic CoAl-LDH on BiVO4 for enhanced photoelectrochemical water oxidation activity, Appl. Catal. B-Eviromen 286 (2021), 119875, https://doi.org/ 10.1016/j.apcatb.2021.119875.

[24] K. Song, F. He, E. Zhou, L. Wang, H. Hou, W. Yang, Boosting solar water oxidation activity of BiVO4 photoanode through an efficient in-situ selective surface cation exchange strategy, J. Energy Chem. 68 (2022) 49–59, https://doi.org/10.1016/j. jechem.2021.11.024.

[25] Y. Song, X. Zhang, Y. Zhang, P. Zhai, Z. Li, D. Jin, J. Cao, C. Wang, B. Zhang, J. Gao, L. Sun, J. Hou, Engineering MoOx/MXene hole transfer layers for unexpected boosting photoelectrochemical water oxidation, Angew. Chem. Int. Ed. 61 (2022), e202200946, https://doi.org/10.1002/anie.202200946.

[26] Y. Lu, Y. Yang, X. Fan, Y. Li, D. Zhou, B. Cai, L. Wang, K. Fan, K. Zhang, Boosting charge transport in BiVO4 photoanode for solar water oxidation, Adv. Mater. 34 (2022), e2108178, https://doi.org/10.1002/adma.202108178.

[27] Y. Bi, Z. Zhang, X. Huang, B. Zhang, High-performance and stable BiVO4 photoanodes for solar water splitting via phosphorus-oxygen bonded FeNi catalysts, Energy Environ. Sci. (2022), https://doi.org/10.1039/D2EE00936F.

[28] X. Zhang, P. Zhai, Y. Zhang, Y. Wu, C. Wang, L. Ran, J. Gao, Z. Li, B. Zhang, Z. Fan, L. Sun, J. Hou, Engineering single-atomic Ni-N4-O sites on semiconductor photoanodes for high-performance photoelectrochemical water splitting, J. Am. Chem. Soc. 143 (2021) 20657–20669, https://doi.org/10.1021/jacs.1c07391.

[29] Z.Z. Ma, K. Song, T. Zhang, B. Tang, G. Shao, H.L. Hou, W.Y. Yang, MXenes-like multilayered tungsten oxide architectures for efficient photoelectrochemical water splitting, Chem. Eng. J. 430 (2022), 132936, https://doi.org/10.1016/j. cej.2021.132936.

[30] J. Deng, Y. Li, Y. Xiao, K. Feng, C. Lu, K. Nie, X. Lv, H. Xu, J. Zhong, Improved water oxidation of Fe2O3/Fe2TiO5 photoanode by functionalizing with a hydrophilic organic hole storage overlayer, ACS Catal. 12 (2022) 7833–7842, https://doi.org/10.1021/acscatal.2c01328.

[31] Y. Zhao, H. Xie, W. Shi, H. Wang, C. Shao, C. Li, Unravelling the essential difference between TiOx and AlOx interface layers on Ta3N5 photoanode for photoelectrochemical water oxidation, J. Energy Chem. 64 (2022) 33–37, https:// doi.org/10.1016/j.jechem.2021.04.042.

[32] X. Song, W. Li, D. He, H. Wu, Z. Ke, C. Jiang, G. Wang, X. Xiao, The "midas touch" transformation of TiO2 nanowire arrays during visible light photoelectrochemical performance by carbon/nitrogen coimplantation, Adv. Energy Mater. 8 (2018) 1800165, https://doi.org/10.1002/aenm.201800165.

[33] T. Butburee, Y. Bai, H. Wang, H. Chen, Z. Wang, G. Liu, J. Zou, P. Khemthong, M. Lu Gao Qing, L. Wang, 2D porous TiO2 single-crystalline nanostructure demonstrating high photo-electrochemical water splitting performance, Adv. Mater. 30 (2018) 1705666, https://doi.org/10.1002/adma.201705666.

[34] Z. Yu, H. Liu, M. Zhu, Y. Li, W. Li, Interfacial charge transport in 1D TiO2 based photoelectrodes for photoelectrochemical water splitting, Small 17 (2021), e1903378, https://doi.org/10.1002/smll.201903378.

[35] C. Huang, J. Bian, Y. Guo, M. Huang, R.-Q. Zhang, Thermal vacuum de-oxygenation and post oxidation of TiO2 nanorod arrays for enhanced photoelectrochemical properties, J. Mater. Chem. A 7 (2019) 5434–5441, https:// doi.org/10.1039/C8TA11830B.

[36] Z. Dong, D. Ding, T. Li, C. Ning, Ni-doped TiO2 nanotubes photoanode for enhanced photoelectrochemical water splitting, Appl. Surf. Sci. 443 (2018) 321–328, https://doi.org/10.1016/j.apsusc.2018.03.031.

[37] J. Jing, J. Yang, W. Li, Z. Wu, Y. Zhu, Construction of interfacial electric field via dual-porphyrin heterostructure boosting photocatalytic hydrogen evolution, Adv. Mater. 34 (2022) 2106807, https://doi.org/10.1002/adma.202106807.

[38] J. Chen, Y. Kang, W. Zhang, Z. Zhang, Y. Chen, Y. Yang, L. Duan, Y. Li, W. Li, Lattice-confined single-atom Fe1Sx on mesoporous TiO2 for boosting ambient electrocatalytic N2 reduction reaction, Angew. Chem. Int. Ed. 61 (2022), e202203022, https://doi.org/10.1002/anie.202203022.

[39] H. Wang, X. Li, Y. Jiang, M. Li, Q. Xiao, T. Zhao, S. Yang, C. Qi, P. Qiu, J. Yang, Z. Jiang, W. Luo, A. Universal Single-Atom Coating, Strategy based on tannic acid chemistry for multifunctional heterogeneous catalysis, Angew. Chem. Int. Ed. 61 (2022), e202200465, https://doi.org/10.1002/anie.202200465.

[40] J. Zheng, K. Lebedev, S. Wu, C. Huang, T. Ayvalı, T.-S. Wu, Y. Li, P.-L. Ho, Y.-L. Soo, A. Kirkland, S.C.E. Tsang, High loading of transition metal single atoms on chalcogenide catalysts, J. Am. Chem. Soc. 143 (2021) 7979–7990, https://doi.org/ 10.1021/jacs.1c01097.

[41] X. Zhao, X. Li, D. Xiao, M. Gong, L. An, P. Gao, J. Yang, D. Wang, Isolated Pd atom anchoring endows cobalt diselenides with regulated water-reduction kinetics for alkaline hydrogen evolution, Appl. Catal. B-Eviron. 295 (2021), 120280, https:// doi.org/10.1016/j.apcatb.2021.120280.

[42] Y. Sun, Z. Xue, Q. Liu, Y. Jia, Y. Li, K. Liu, Y. Lin, M. Liu, G. Li, C.-Y. Su, Modulating electronic structure of metal-organic frameworks by introducing atomically dispersed Ru for efficient hydrogen evolution, Nat. Commun. 12 (2021) 1369, 10.1038/s41467-021-21595-5.

[43] Z.-H. Xue, D. Luan, H. Zhang, X.W. Lou, Single-atom catalysts for photocatalytic energy conversion, Joule 6 (2022) 92–133, https://doi.org/10.1016/j. joule.2021.12.011.

[44] K.H. Kim, C.-W. Choi, S. Choung, Y. Cho, S. Kim, C. Oh, K.-S. Lee, C.-L. Lee, K. Zhang, J.W. Han, S.-Y. Choi, J.H. Park, Continuous oxygen vacancy gradient in TiO2 photoelectrodes by a photoelectrochemical-driven "self-purification" process, Adv. Energy Mater. 12 (2022) 2103495, https://doi.org/10.1002/ aenm.202103495.

[45] Y. Han, J. Wu, Y. Li, X. Gu, T. He, Y. Zhao, H. Huang, Y. Liu, Z. Kang, Carbon dots enhance the interface electron transfer and photoelectrochemical kinetics in TiO2 photoanode, Appl. Catal. B-Environ. 304 (2022), 120983, https://doi.org/ 10.1016/j.apcatb.2021.120983.

[46] A.M. Hamisu, A. Ariffin, A.C. Wibowo, Cation exchange in metal-organic frameworks (MOFs): The hard-soft acid-base (HSAB) principle appraisal, Inorg. Chim. Acta 511 (2020), 119801, https://doi.org/10.1016/j.ica.2020.119801.

[47] H. Zhang, S. Zuo, M. Qiu, S. Wang, Y. Zhang, J. Zhang, X.W. Lou, Direct probing of atomically dispersed Ru species over multi-edged TiO2 for highly efficient photocatalytic hydrogen evolution, Sci. Adv. 6 (2020), eabb9823, https://doi.org/ 10.1126/sciadv.abb9823.

[48] M. Xiao, L. Zhang, B. Luo, M. Lyu, Z. Wang, H. Huang, S. Wang, A. Du, L. Wang, Molten-salt-mediated synthesis of an atomic nickel co-catalyst on TiO2 for improved photocatalytic H2 evolution, Angew. Chem. Int. Ed. 59 (2020) 7230–7234, https://doi.org/10.1002/anie.202001148.

[49] J.-X. Guo, D.-Y. Yan, K.-W. Qiu, C. Mu, D. Jiao, J. Mao, H. Wang, T. Ling, High electrocatalytic hydrogen evolution activity on a coupled Ru and CoO hybrid electrocatalyst, J. Energy Chem. 37 (2019) 143–147, https://doi.org/10.1016/j. jechem.2018.12.011.

[50] S. Wang, T. He, P. Chen, A. Du, K. Ostrikov, W. Huang, L. Wang, In situ formation of oxygen vacancies achieving near-complete charge separation in planar BiVO4 photoanodes, Adv. Mater. 32 (2020) 2001385, https://doi.org/10.1002/ adma.202001385.